Supporting Information

Two dimensional chalcogenide nanoplates as tunable metamaterials via chemical intercalation

Judy J. Cha[1], Kristie J. Koski[1], Kevin C.Y. Huang[2], Ken Xingze Wang[3], Weidong Luo[4], Desheng Kong[1], Zongfu Yu[2], Shanhui Fan[2], Mark L. Brongersma[1,4], Yi Cui[1,4,5*]*

[1] Department of Materials Science and Engineering, Stanford University, Stanford, CA 94305, USA.

[2] Department of Electrical Engineering, Stanford University, Stanford, CA 94305, USA.

[3] Department of Applied Physics, Stanford University, Stanford, CA 94305, USA.

[4] Geballe Laboratory for Advanced Materials, Stanford University, Stanford, CA 94305, USA.

[5] Stanford Institute for Materials and Energy Sciences, SLAC National Accelerator Laboratory, 2575 Sand Hill Road, Menlo Park, CA 94025, USA.

*Correspondence to: YC, email: yicui@stanford.edu and MLB, brongersma@stanford.edu.

Methods

Materials synthesis: Bi_2Se_3 nanomaterials were synthesized by hydrothermal synthesis, vapor-solid (VS) growth, and vapor-liquid-solid (VLS) growth, following the procedures and set-ups reported elsewhere[1, 2]. Here, we provide brief descriptions. To synthesize Sb-doped Bi_2Se_3 nanoplates hydrothermally, polyvinylpyrrollidone (0.5g from Sigma Aldrich), ethylene diamene tetraacetic acid (1g from Sigma Aldrich), Bi_2O_3 (1mmol from Sigma Aldrich), antimony acetate (0.30g from Alfa Aesar), and selenium powder (3mmol from Aldrich) were added into ethylene glycol (40ml; from EMD) and stirred vigorously for two hours at 35°C. The solution was transferred into a Teflon lined stainless steel autoclave and heated at 165°C for 8-12 hours. Nanoplates were collected by centrifugation at 1700 rpm for 10 min, washed several times with ethanol, and re-dispersed in ethanol.

For VS and VLS growth, the Bi_2Se_3 source powder (99.999%, Alpha Aesar) was placed in the hot center (530 °C) of a tube furnace. At colder zones (~ 350 – 450 °C), SiO_x substrates (for nanoplates) or Si substrates decorated with Au particles (for nanoribbons) were placed. During growth, high purity Ar gas was flowed through the furnace at ~ 120 standard cubic centimeters at ~ 1 Torr for 2-3 hrs. Alloy chalcogenides, $Bi_2(Se_xTe_{1-x})_3$ and $(Sb_xBi_{1-x})_2Te_3$, were synthesized in the same way except that the source powder was a mixture of two binary compounds (Bi_2Se_3 and Bi_2Te_3, or Sb_2Te_3 and Bi_2Te_3). For optimal growth conditions, please refer to previous reports[3, 4].

Intercalation: Intercalation of organic molecules into metal chalcogenides has been extensively studied in the past, and well-established intercalation recipes can be found in the literature. We followed a typical intercalation method for this study[5-8]. For intercalation of pyridine, nitrobenzene, and dodecylamine into Bi_2Se_3 nanoplates and nanoribbons, silicon substrates

containing nanoribbons or SiN_x TEM grids containing nanoplates were immersed in the intercalant solution. The solution was then heated and kept at reflux for 20 – 28 hours. After intercalation, samples were washed with methanol or acetone to remove excess, residual molecules. By observing the same nanoplates placed on SiN_x TEM grids, changes in the photonic modes of Bi_2Se_3 induced by intercalation were directly observed. In the case of dodecylamine intercalation, direct comparison before and after intercalation was difficult because excess dodecylamine could not be completely removed from the SiNx membrane. For intercalation of copper metal, we followed the procedure we reported previously[5].

Direct comparison of the same plate before and after intercalation is preferred to comparing two different batches of the sample, one pristine and the other intercalated for several reasons. First, intercalation introduces volume expansion to the host material. Thus, unless we compare the same plate, we cannot rule out thickness effects. Second, by looking at the same sample after intercalation, we minimize variation in background EELS signal coming from the SiNx TEM grid. Third, only by looking at the same plate before and after, we can do direct comparison of the changes in EELS due to intercalation. To make sure that residual molecules will not influence the EELS spectra, the samples were thoroughly washed off with acetone or ethanol after intercalation.

Experimental Set-up: An aberration-corrected FEI Titan microscope at 300 kV in monochromated mode was used for the study. A single shot zero-loss peak in monochromated mode achieves 0.13 eV full width at half maximum. For pristine Bi_2Se_3 nanoplate studies, the plates were drop-cast on quantafoil TEM grids, so that regions of the plates suspended in vacuum could be investigated, avoiding background signals from the support films. For pyridine and nitrobenzene intercalation studies, nanoplates were drop-cast on SiN_x TEM grids so that we

could follow the same plates before and after intercalation. For the thickness calibration, nanoplates on SiN_x TEM grids were studied with EELS, followed by thickness measurements using atomic force microscopy.

Simulation Details: Simulations were performed with full-field finite-difference time-domain (FDTD) in the two-dimensional transverse magnetic polarization (2D TM) where the magnetic field was out of the Bi_2Se_3 basal plane, and electric field in-plane to the Bi_2Se_3 basal plane. The electron beam was approximated with a point broadband electric dipole source oscillating in the vertical direction placed 8 nm above the Bi_2Se_3 film surface. The energy loss was calculated by integrating the steady-state Poynting vector around a closed surface enclosing the dipole source as a function of frequency via Fast Fourier Transform. The final quantity was normalized by the total power emitted from the dipole placed in homogeneous air medium. This calculation is equivalent to computing the local density of optical states at the location of the electric dipole. It is also equivalent to the spontaneous emission rate enhancement or the Purcell factor of the dipole. Despite the fact that this calculation does not take into account the relativistic speed of the electron or other physical effects of a swift electron, it has been demonstrated to give excellent agreement with experimentally measured transition radiation excited by an electron beam impinging on a thin metal film in a cathodoluminescence setup[9].

The plasmon intensity map at 3.9 eV of a 10-nm thick rectangular Bi_2Se_3 film, shown in Fig. 1i, is obtained by moving the location of the electric dipole over a 250 nm by 250 nm area at 5 nm step resolution and calculating the corresponding local density of the optical states at 3.9 eV.

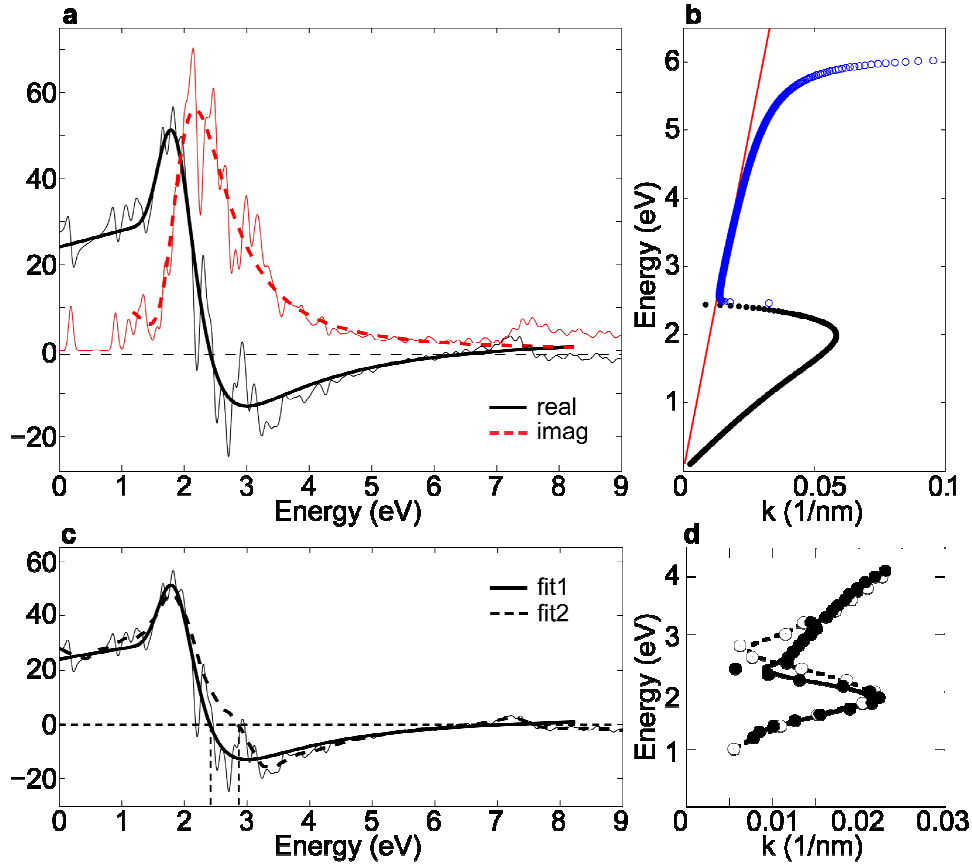

Fig. S1. **Calculated dielectric constant of bulk Bi_2Se_3 and dispersion of the surface plasmon and photonic guided mode. a,** The dielectric constant was obtained by Kramers-Kronig analysis of the electronic band structure of bulk Bi_2Se_3, obtained by first-principle calculation using VASP. The thicker lines are smoothed fits that were used for the FDTD calculations of the surface plasmon and the photonic guided modes. We note that the exact amplitude of the dielectric constant of Bi_2Se_3 nanoplates may differ slightly from the calculation. However, the trend is clear that the dielectric constant is a large positive number in infrared and negative in ultraviolet. **b,** As a first approximation, surface plasmon dispersion (blue) and light dispersion inside Bi_2Se_3 (black) were calculated from the dielectric function, using the following equations:

$k = \frac{\omega}{c_o}\sqrt{\frac{\varepsilon_1\varepsilon_2}{\varepsilon_1+\varepsilon_2}}$ for surface plasmon and $c(k)_{Bi_2Se_3} = c_o/n$ where $n = \sqrt{\frac{\sqrt{\varepsilon_1^2+\varepsilon_2^2}+\varepsilon_1}{2}}$ for the

photonic mode. ω is the plasmon frequency, c_o is the speed of light in vacuum, and ε_1 and ε_2 are the real and imaginary part of the dielectric function. The red line is a light line in vacuum (ω=ck). **c,** Two smooth fits to the real part of the dielectric function from the first-principle calculation. The solid thick line (fit 1) is the same curve as the one shown in **a**, while the dotted thick line (fit 2) is a smooth fit in which the real part of the dielectric constant crosses zero at 2.8 eV. The zero-crossing at 2.8 eV in fit 2 is to reflect the experimental observation more closely; experimentally, we observe that the dielectric photonic mode goes up to ~ 3 eV. **d,** Dispersion curves of a 10-nm thick Bi_2Se_3 slab, using the two smooth fits of the real part of the dielectric function, shown in **c**. The solid and open dots represent dispersion curves obtained using fit 1 and fit 2 respectively. The solid dot dispersion is identical to the one shown in Fig. 1h. Using fit 2, the calculated dispersion curve matches the experimental observation, shown in Fig. 1g, more closely.

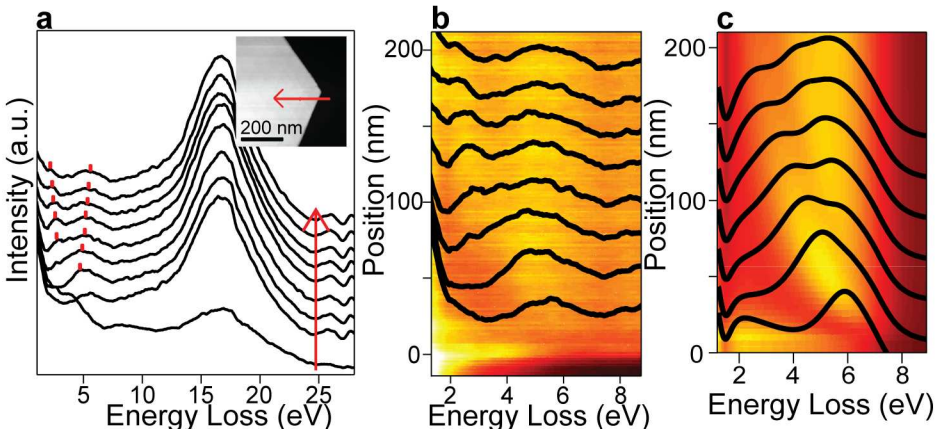

Fig. S2. Spectral imaging of photonic and plasmonic modes. a, EELS line profile at the ~ 16 nm-thick Bi_2Se_3 plate edge. Spectra are acquired from equally spaced spots along the red line (inset) and displayed with an offset for visual clarity (not all spectra are shown). Bottom-most spectrum is from the right end of the red line. The peak at 2.5 eV shifts to higher energy near the edge of the plate, finally merging with the peak at 5 eV. The red dots are visual guide. **b,** 2D color plot of the EELS line profile in **a**, overlaid with spectra acquired at 26, 51, 77, 102, 128, 153, 179, and 204 nm away from the plate edge (0 nm). The color represents intensity, and spatial variations of the peak intensities are clear in this plot. Horizontal line cuts give individual spectra, shown in **a**. **c,** Calculated 2D color plot of modal excitations across the edge of a 10 nm-thick semi-infinite Bi_2Se_3 film. Calculated spectra at positions equal to experimental positions are overlaid in the color plot.

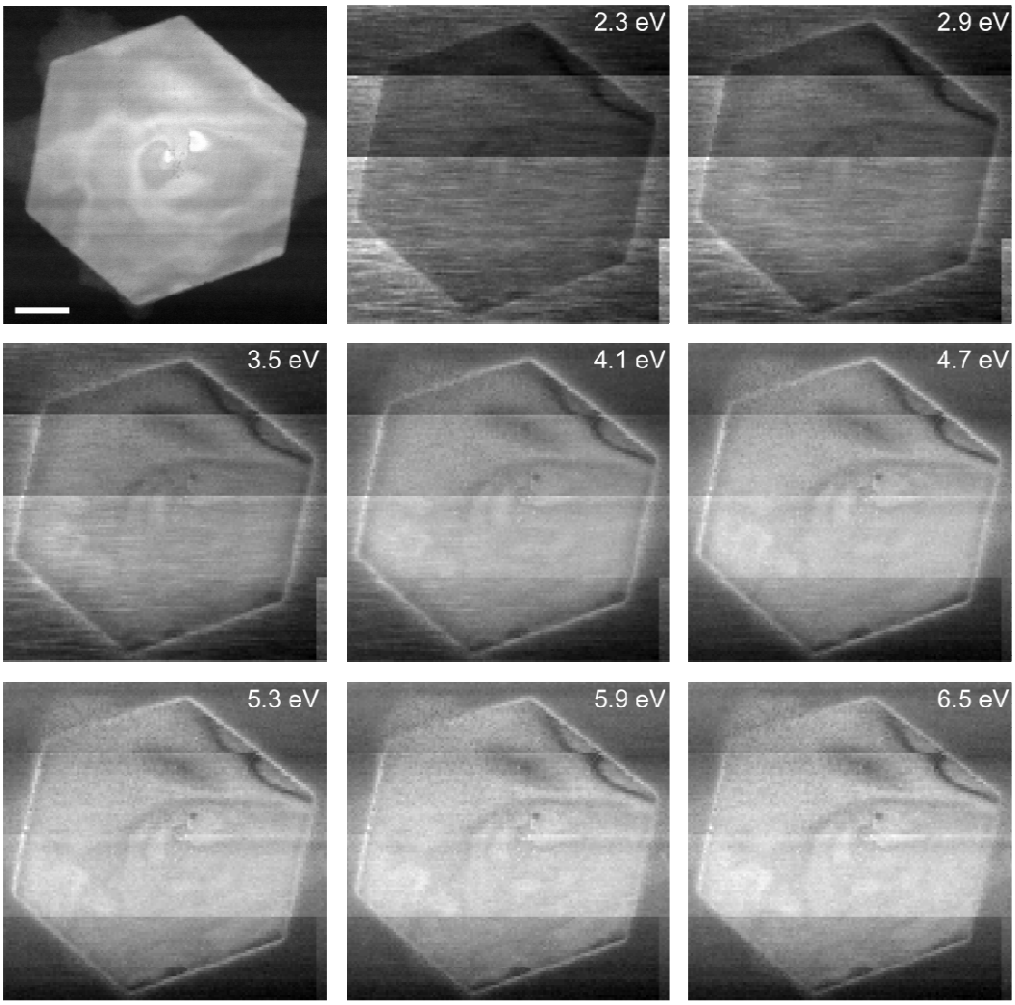

Fig. S3. **Plasmon maps at several energies of a small Bi_2Se_3 nanoplate, sitting on a SiN_x membrane TEM grid.** Top, left panel shows an annual dark field STEM image of the plate. Scale bar is 100 nm. The rest are 128 x 128 pixel maps, acquired from integrating EEL spectra at each pixel over a 0.3 eV window at particular energies. Four 32 x 128 pixel spectral images were combined to produce this 128 x 128 pixel maps. The interference pattern of the surface plasmon is clearly demonstrated by the dark region which gradually shrinks at higher plasmon energies. The intensity variation in the images may come from inhomogeneous coverage of an organic layer residue, left over from the hydrothermal synthesis, and the local bending of the

plate as the suspended SiN_x membrane is not completely flat. Supplementary Movie S2 plays the sequential frames of the plasmon maps.

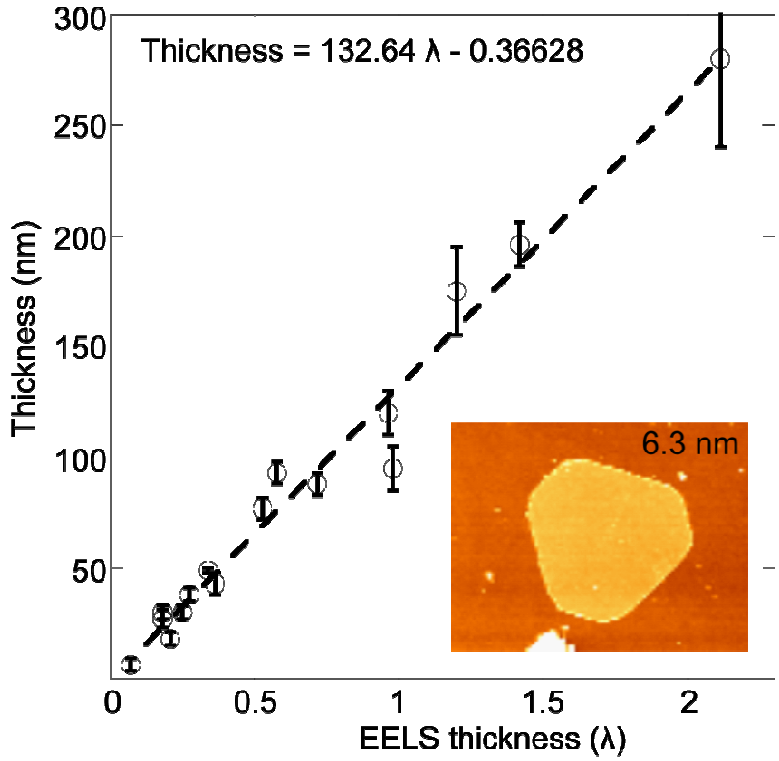

Fig. S4. **Thickness calibration of Bi_2Se_3 nanoplates.** Plate thicknesses were obtained from the calibration curve shown above. First, the thicknesses were measured using atomic force microscopy (AFM) on plates and ribbons that were sitting on SiN_x membrane TEM grids. The inset shows an AFM image of one such plate whose thickness is 6.3 nm. Then, EELS were acquired from the same plates and ribbons, where the relative thicknesses in units of the mean free path (λ) were calculated by taking the log ratio of the zero-loss peak intensity to inelastically scattered peak intensity in the low-loss region[10]. Digital micrograph was used for the calculation. As shown above, the absolute thickness measured by AFM linearly scales with the relative thickness obtained from EELS, resulting in a reliable calibration curve. For this calibration curve, the mean free path from the SiN_x membrane was subtracted. For plates that were

suspended over holey carbon films, their thicknesses were estimated using the calibration curve. We note that in very thin plates, this calibration curve may not produce accurate thickness information as the surface plasmon coupling effects and other thin film effects such as contamination layers will influence the low-loss EELS spectra[10, 11].

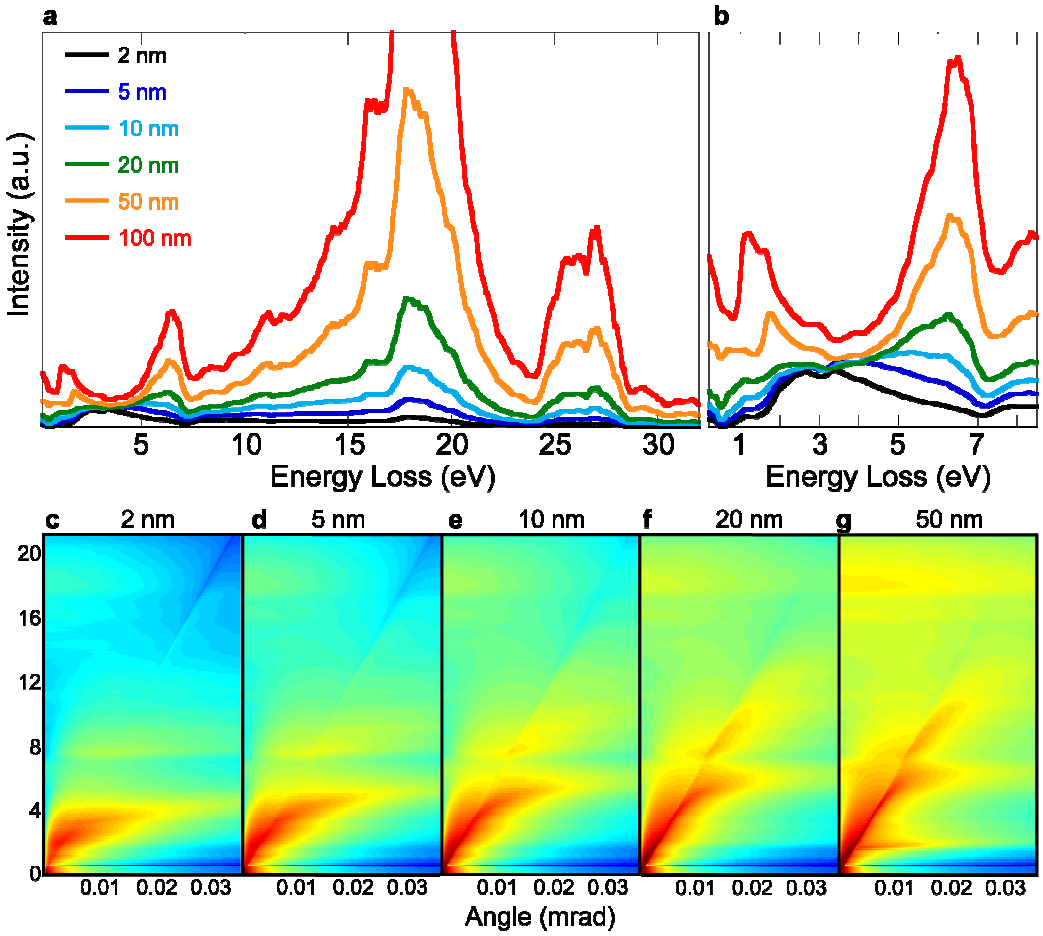

Fig. S5. **Calculated EELS loss functions and dispersions of Bi_2Se_3 nanoplates of varying thicknesses. a,** EELS loss functions were simulated by exciting laterally infinite Bi_2Se_3 slabs with 300 keV swift electrons, and integrating the energy loss scattering events up to a collection angle of 80 mrad. Retardation effects such as Cherenkov radiation[12] were fully included in the simulation using Kroger's formalism [13]. All plasmon excitations (~ 7, 17, 26-28 eV) in the calculated EELS loss functions match well with the experimental results. **b,** A zoom-in in the low energy loss region below 8 eV. The plasmon at ~ 6.8 eV systematically shifts to a lower energy in thinner slabs due to the surface plasmon coupling, in agreement with the EELS experimental results and FDTD calculations. The growing peak at ~1.4 eV in thicker slabs is the photonic guided mode, which blue-shifts in thinner slabs in agreement with the experiment. **c-g,**

Calculated dispersion maps at slab thicknesses ranging from 2 nm to 50 nm. At the slab thickness of 50 nm, the photonic guided mode is prominent.

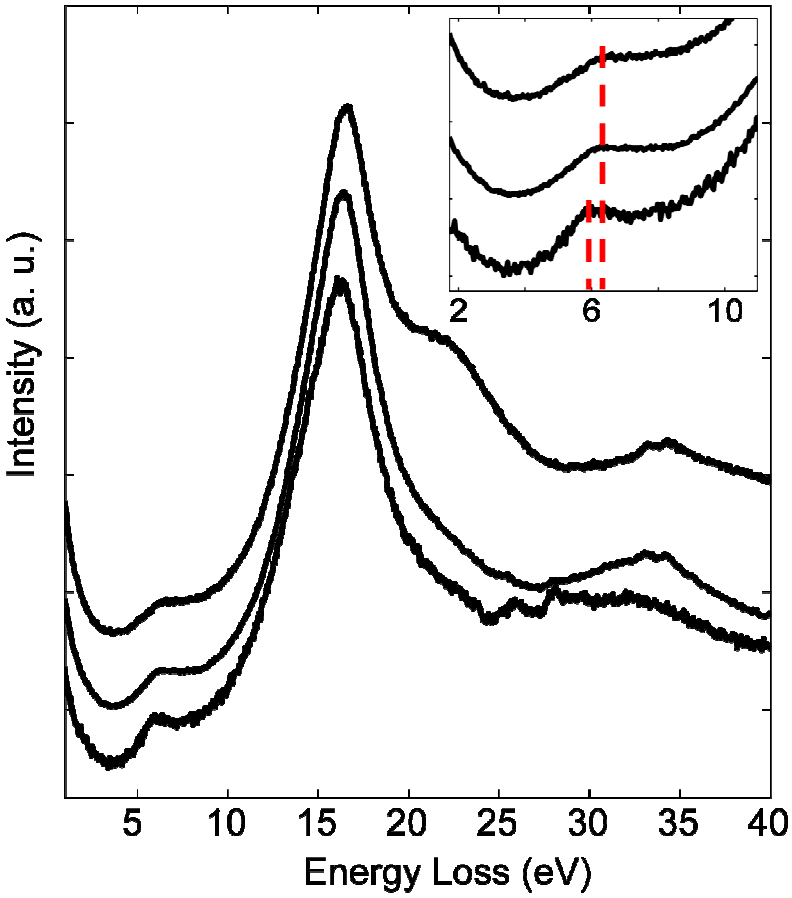

Fig. S6. **Changes in plasmon energies in thick $(Sb_xBi_{1-x})_2Te_3$ nanoplates with varying ratio, x.** EELS spectra from three compositions were measured: Sb_2Te_3 (top), $(Sb_2Te_3)_{0.5}(Bi_2Te_3)_{0.5}$ (middle), and Bi_2Te_3 (bottom). Although small, the plasmon at ~ 6 eV shifts to higher energies with increasing x, as indicated by the dotted red lines in the zoom-in inset. The average plasmon energies are 5.92 eV for Bi_2Te_3, 6.17 eV for $(Sb_2Te_3)_{0.5}(Bi_2Te_3)_{0.5}$, and 6.19 eV for Sb_2Te_3.

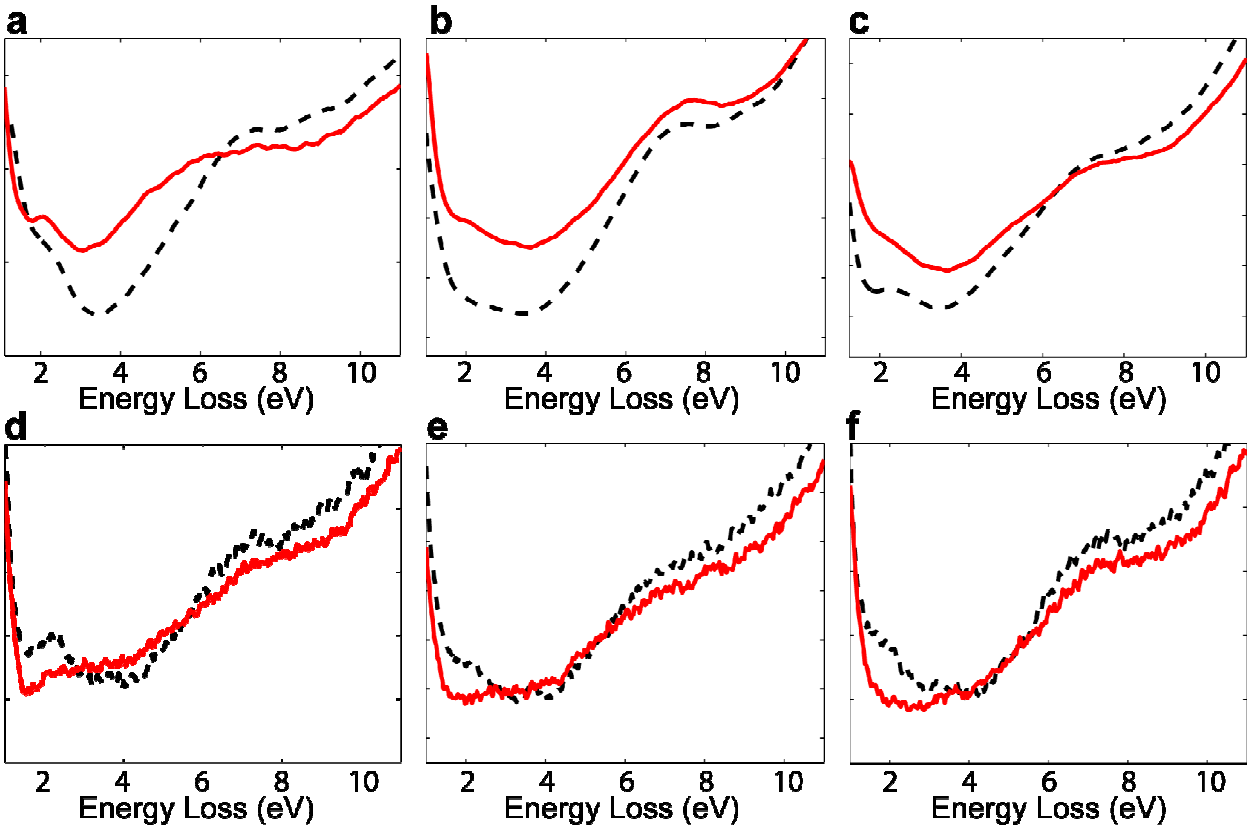

Fig. S7. **Changes in the photonic mode after pyridine and nitrobenzene intercalation in Bi_2Se_3 nanoplates**. **a-c,** Pyridine-intercalated Bi_2Se_3 nanoplates, showing clear changes in EELS before (dotted black) and after (solid red) the intercalation. The intensity of the photonic modes is enhanced in all three plates, showing the same trend as the one shown in Fig. 4a. **d-f,** Nitrobenzene-intercalated Bi_2Se_3 nanoplates, showing clear changes in EELS before (dotted black) and after (solid red) the intercalation. The intensity of the photonic modes is decreased in all three plates, showing the same trend as the one shown in Fig. 4b. For these comparisons before and after intercalation, EELS were normalized to the bulk plasmon peak of Bi_2Se_3 at ~ 17 eV.

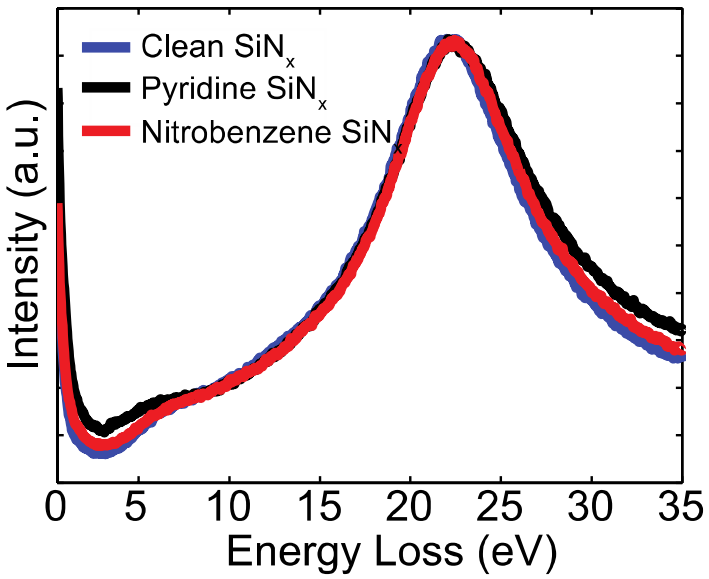

Fig. S8. **EELS background signal comparison from the SiN_x membrane between pristine SiN_x and intercalation-treated SiN_x membranes**. To make sure that changes in EELS after intercalation were due to the intercalants inserted into Bi_2Se_3 nanoplates (Fig. 4 in the main text and Fig. S7), the samples were thoroughly washed off with acetone or ethanol after intercalation to remove residual molecules. Background EELS data from pristine SiN_x membrane, pyridine-intercalation treated SiN_x membrane, and nitrobenzene-intercalation treated SiN_x membranes are compared. The EELS spectra overlap nicely within the variability of the SiN_x membranes (primarily thickness differences). This shows that residual molecules were thoroughly washed off and did not contribute to the changes in EELS after intercalation.

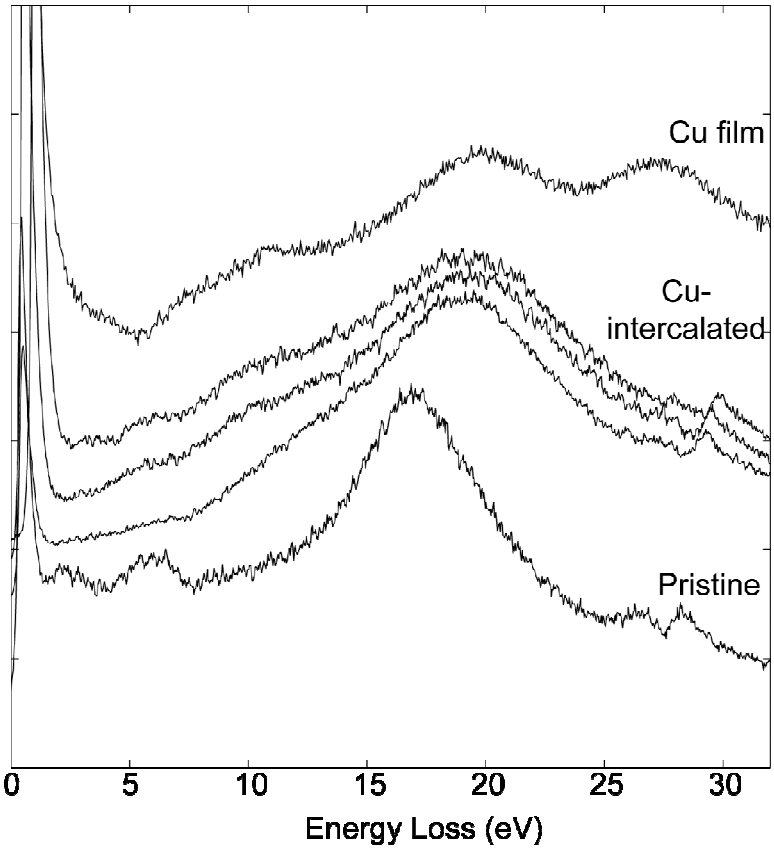

Fig. S9. **Changes in plasmonic modes after copper (Cu) intercalation in Bi_2Se_3 nanoplates.** EELS from ~ 40% Cu-intercalated Bi_2Se_3 nanoplates (three spectra in the middle) are clearly different from pristine Bi_2Se_3 nanoplates (the bottom spectrum and Fig. 1 in the main text). The photonic mode and surface plasmon appear much suppressed in Cu-intercalated Bi_2Se_3 nanoplates. The thicknesses of Cu-intercalated plates are comparable to the pristine nanoplates. As a reference, EELS of a 30 nm-thick Cu film is also shown (top spectrum). Care was taken during intercalation to make sure no Cu particles were formed inside or on the surface of Cu-intercalated Bi_2Se_3 nanoplates[5].

References

1. Kong, D.; Dang, W.; Cha, J. J.; Li, H.; Meister, S.; Peng, H.; Liu, Z.; Cui, Y. *Nano Letters* **2010,** 10, 2245-2250.
2. Kong, D.; Randel, J. C.; Peng, H.; Cha, J. J.; Meister, S.; Lai, K.; Chen, Y. L.; Shen, Z. X.; Manoharan, H. C.; Cui, Y. *Nano Letters* **2010,** 10, (1), 329-333.
3. Kong, D.; Chen, Y.; Cha, J. J.; Zhang, Q.; Analytis, J. G.; Lai, K.; Liu, Z.; Hong, S. S.; Koski, K. J.; Mo, S.-K.; Hussain, Z.; Fisher, I. R.; Shen, Z.-X.; Cui, Y. *Nat Nano* **2011,** 6, (11), 705-709.
4. Cha, J. J.; Kong, D.; Hong, S.-S.; Analytis, J. G.; Lai, K.; Cui, Y. *Nano Letters* **2012,** 12, 1107-1111.
5. Koski, K. J.; Cha, J. J.; Reed, B. W.; Wessells, C. D.; Kong, D.; Cui, Y. *Journal of the American Chemical Society* **2012,** 134, (18), 7584-7587.
6. Koski, K. J.; Wessells, C. D.; Reed, B. W.; Cha, J. J.; Kong, D.; Cui, Y. *J Am Chem Soc* **2012,** 134, 13773.
7. Friend, R. H.; Yoffe, A. D. *Advances in Physics* **1987,** 36, (1), 1-94.
8. Parry, G. S.; Scruby, C. B.; Williams, P. M. *Philosophical Magazine* **1973,** 29, (3), 601-612.
9. Barnard, E. S.; Coenen, T.; Vesseur, E. J. R.; Polman, A.; Brongersma, M. L. *Nano Letters* **2011,** 11, (10), 4265-4269.
10. Egerton, R. F., *Electron Energy-Loss Spectroscopy in the Electron Microscope*. Plenum Press: New York, 1996.
11. Ritchie, R. H. *Physical Review* **1957,** 106, (5), 874.
12. Cherenkov, P. *Dokl. Akad. Nauk SSSR* **1934,** 2, 451.
13. Kroger, E. *Zeitschrift Fur Physik* **1968,** 216, 115-135.